

## Contents

<b>1.</b>	<b>Experimental details for the steel sphere cooling experiments</b>	<b>2</b>
1.1	Hydrophilic spheres	2
1.2	Superhydrophobic spheres	3
1.3	Superhydrophilic spheres	4
1.4	Hydrophobic spheres	4
1.5	Sphere cooling experiments	5
1.6	Sphere cooling in heated water	5
1.7	Varying hydrophobicity and Cytronix coating	7
<b>2.</b>	<b>Experimental details for the heating devices experiments</b>	<b>8</b>
2.1	Immersion heater device and measurement protocol	8
2.2	Experiments with superhydrophobic heater	10
2.3	Experiments with superhydrophilic, hydrophilic and hydrophobic heater	10
2.4	Steel cup container experiments	11
2.5	Leidenfrost droplet evaporation experiments	12
<b>3.</b>	<b>Stabilization of the vapour phase due to surface texture</b>	<b>14</b>
3.1	Nanoparticle scale roughness	15
3.2	Coarse scale roughness	17
	<b>References</b>	<b>19</b>
	<b>Supplementary Movie Legends</b>	<b>20</b>
	<b>Supplementary Figures and Legends</b>	<b>21-43</b>

## 1 Experimental detail for the steel sphere cooling experiment

The spheres used were polished stainless steel grinding balls (FRITSCH GmbH) of density  $\rho_s = 7.7 \text{ g/cm}^3$  and diameter,  $d = 20 \text{ mm}$ . The average surface roughness given by the manufacturer is  $R_a < 0.06 \text{ }\mu\text{m}$ . Descriptions of how the surfaces of the sphere were made to be superhydrophilic, hydrophilic, hydrophobic and superhydrophobic are given in sections 1.1 to 1.4. Different cooling experiments are described in sections 1.5 to 1.7.

### 1.1 Hydrophilic spheres

After washing with acetone, ethanol and water, the spheres have an apparent contact angle with water drops of less than  $10^\circ$ . The clean, unmodified spheres are referred as ‘hydrophilic’ spheres.

Using a tungsten carbide drill bit we drilled a 1.5 mm diameter hole into the top of the spheres down to the sphere center. This allowed us to mount a holding stake for easy handling of the spheres and for surface modification without touching the sphere surface. For experiments where the sphere temperature was measured, the holding stake was a thermocouple probe.

The clean spheres have a shiny silver-white appearance. Heating the spheres to about  $400^\circ\text{C}$  changes the sphere’s colour to bronze-brown (Fig. 3a) and further heating to  $700^\circ\text{C}$  changes the colour again to purple-blue. The sphere colour change is due to the heat-induced oxidation of the steel surface layer. The oxide layer did not affect the sphere wettability significantly. After heating, the spheres remain hydrophilic with apparent water contact angle of no more than  $30^\circ$ .

## 1.2 Superhydrophobic spheres

The superhydrophobic spheres were prepared using a commercially available coating agent (Glaco Mirror Coat “Zero”, Soft 99 Co.). It is a car mirror water-repellant agent used to keep the car side vision mirrors clean during rain, even at “zero” car speed. As advertised on the company web-site (<http://www.soft99.co.jp/en/>): “The repellent prevents water from remaining on the surface even for a moment by lining the mirror with super-fine, microscopic studs“. The agent is sold in aerosol form for spraying on the mirror, but Soft99 has kindly provided us with the liquid form of the aerosol product. The product ingredients listed by the manufacturer are alcohol and silica, from which we assume that this is an alcohol-based suspension of silica nanoparticles functionalized by organic hydrophobizing agent. We characterized the coating topology using atomic force microscopy (AFM) and scanning electron microscopy (SEM) imaging. Fig. 1a shows a  $2 \mu\text{m}^2$  AFM topological images of the coating deposited on a flat silica wafer surface. Fig. 1b shows a larger  $35 \mu\text{m}^2$  AFM image and Fig. 1c is a high resolution SEM image. The images indicate that the characteristic particle size of the coating is 40 to 60 nm (Fig. 1a, Fig. 1c). On a large-scale the coating has self-assembled nanoparticles that form a fractal-type structure with a coarse scale pillar-type roughness ranging from 0.1-2 micron spacing and 50-300 nm depth (Fig. 1a-c).

The superhydrophobic coating was applied on the clean surface steel spheres by pouring the Glaco coat liquid over the sphere (washing the spheres with the agent). A thin liquid film wets the sphere surface and dry in less than a minute. After the first application of Glaco we heat cure the sphere at  $300 \text{ }^\circ\text{C}$  for half an hour, then repeat the application and heat-curing process three to four times. The spheres retain their hydrophobicity upon heating to about  $400 \text{ }^\circ\text{C}$ .

Following the above procedure the sphere superhydrophobicity is excellent. It becomes challenging to deposit a static water droplet (1 to 3 mm diameter) on the sphere surface as the droplet easily rolls away. Water droplets readily bounce from the sphere surface when

released from a small height as illustrated in the video sequence shown in Fig. 2e–h. As shown on Fig. 2a–d, fixing a syringe connected glass pipette near the top of the sphere allows us to measure the advancing and receding contact angles of an millimetric water droplet, with advance contact angle of about  $170^\circ$  (Fig. 2a) and receding contact angle close to  $160^\circ$  (Fig. 2b). When the superhydrophobic spheres are immersed under water, a silver-mirror-like sheen of the sphere can be observed (Fig. 3b and manuscript Fig. 1c). This sheen is due to the reflection of light from the thin air layer retained on the sphere surface during immersion and is signature of a Cassie-Baxter state. The same sheen is observed during the sphere cooling in Leidenfrost regime (Fig. 3c) and after the complete cooling of the heated superhydrophobised spheres (Fig. 3d).

Another commercial agent Cytronix PFC 1604V has also been used to produce superhydrophobic surfaces – see section 1.7.

### 1.3 Superhydrophilic spheres

To yield superhydrophilic spheres, the spheres were initially coated with the Glaco superhydrophobic coating and were then subjected to plasma cleaning. The initial Glaco coating was applied in the same manner as in the previous section. The plasma treatment of the coated spheres lasted for approximately 5 minutes using a plasma-cleaner device (Harrick PDC-002). This overall procedure resulted in superhydrophilic surface with water contact angles of less than  $10^\circ$ . The plasma cleaning essentially decomposes the organic hydrophobizing agent, thus exposing the surface of the hydrophilic silica nanoparticles. SEM images of the coating before and after the plasma treatment confirmed that the coating morphology is not affected by the plasma treatment (Fig. 1c and 1d).

### 1.4 Hydrophobic spheres

Steel spheres were hydrophobized by silanization with a silane reagent ((Trichloro (1H, 1H, 2H, 2H perfluorooctyl) silane, 97% Aldrich)). To improve the silane deposition, the spheres

were pre-treated using the plasma-cleaning device. The sphere was then placed in a desiccator together with an open vial containing several drops of the reagent. The desiccator is closed and evacuated to low vacuum for about half an hour to carry out the vapor phase deposition of the agent on the sphere surface. After silanization the advancing contact angle of a water droplet on the sphere surface is about  $115^\circ$  (Fig. 2c) and the receding contact angle is about  $85^\circ$  (Fig. 2d). The coating is stable upon heating to about  $380^\circ\text{C}$ .

### 1.5 Sphere cooling experiments

A schematic of the setup for the sphere heating and water-cooling experiments is shown in Fig. 4. First the sphere was heated in a temperature control muffle furnace (Thermo Scientific). It was convenient to hang the sphere into the furnace through the furnace ventilation opening at the top as schematized in Fig 4a. We used a K-type thermocouple probe (TJ36-CASS-116E-6-CC, Omega Engineering) connected to a thermocouple thermometer (OM-SQ2010-KIT, Omega Engineering) to monitor the temperature in the sphere center. After heating the sphere to the desired temperature the sphere probe was immersed in the water filled glass wall tank ( $20\times 20\times 50$  cm, Fig. 4b) to a depth of about 3 to 4 cm below the water surface. The sphere cooling was recorded with a high-speed video camera (Photron Fastcam SA-5). The thermocouple thermometer was connected to a PC from which the sphere temperature was sampled at frequency of 10 Hz.

### 1.6 Sphere cooling in heated water

Data for the sphere cooling in room temperature water are given in Fig. 3 of the manuscript. Additional cooling experiments were performed to investigate the sphere cooling rate in heated water. The cooling was carried out in a 1-liter Pyrex glass beaker placed on a temperature controlled stirrer/hot plate. Results for the sphere cooling in water at  $80^\circ\text{C}$  and  $100^\circ\text{C}$  are shown in Fig. 5a for the superhydrophilic sphere, Fig. 5b for the hydrophilic

sphere, Fig. 5c for the hydrophobic sphere and Fig 5d for the superhydrophobic sphere. These experiments follow the same trends with respect of the sphere hydrophobicity as the room-temperature cooling experiments. As can be expected, increasing the water temperature decreases the initial cooling rates and lowers the Leidenfrost transition temperatures.

For the superhydrophilic sphere cooling in 80 °C water, the initial sphere temperature of 800 °C is still below the Leidenfrost temperature,  $T_L$  for this case and the sphere makes immediate physical contact with water resulting in fast cooling in nucleate regime (Fig. 5a, blue line). For the superhydrophilic sphere cooling in 100 °C water, the sphere, initially at 800 °C, starts cooling in the Leidenfrost regime to reach the Leidenfrost point (LP) at  $T_L$  of about 700 °C (Fig. 5a, red line). Due to the relevantly high  $T_L$  in that case, following the layer break-up marked by an abrupt temperature drop, the sphere cooling rate is slowed by large bubbles that formed around the sphere (transition boiling, Fig. 5a) before the final cooling rate increase in the nucleate boiling regime.

For the hydrophilic sphere cooling in 80 °C water,  $T_L = 270$  °C and for 100 °C water,  $T_L = 254$  °C (Fig. 5b). For the hydrophobic sphere in 80 °C water,  $T_L = 170$  °C and for 100 °C water  $T_L = 125$  °C (only 25 °C of superheat), but a Leidenfrost transition is still clearly observed (Fig. 5c). Thus the cooling behaviors of superhydrophilic, hydrophilic and hydrophobic are all similar qualitatively – initially with a slow Leidenfrost cooling regime until reaching the Leidenfrost temperature and then changing to a fast nuclear boiling regime.

In contrast to the previous three surface treatments, the cooling behavior of the superhydrophobic sphere is qualitatively different. The sphere temperature gradually approaches the pool temperature for both cooling in 80 °C and 100 °C water without transition to nucleate boiling (Fig. 5d) and the final appearance of the sphere is shiny indicating that the vapor layer relaxes to the Cassie state (Fig. 3d and manuscript Fig. 2b).

The sphere temperature vs. time dependence can be used to estimate the heat flux dependence on the surface superheat temperature. The instantaneous heat flux,  $q$  from the sphere of radius  $R$  is calculated on the basis of the lumped-capacity approach by assuming the sphere temperature,  $T_S$  to be uniform. The immediate heat flux is then given by<sup>1</sup>:

$$q = \rho c R (dT_S / dt) / 3 \quad (\text{S1})$$

where  $\rho = 7.8 \text{ g/cm}^3$  is the sphere density,  $c = 460 \text{ J/kgK}$  is the sphere specific heat. Fig. 6a shows heat flux vs. sphere temperature calculated from the 100 °C water data for the hydrophilic sphere (blue line) and for the superhydrophobic sphere (red line) and Fig. 6b shows the zoomed-in region of low heat flux for the same data.

### 1.7 Varing hydrophilicity and Cytronix coating

Fig. 7 shows the variation in Leidenfrost temperatures with the surface contact angle for the case of smooth (blue squares) and textured (red squares) surfaces. The presented data are for a sphere cooling in 100 °C water. The wettability of the spheres was adjusted by varying the plasma treatment time (between 10 to 120 seconds) of the hydrophobic or superhydrophobic (Glaco coating) spheres. The short-time plasma treatment partially degrades the hydrophobizing agent, giving the possibility to vary the surface hydrophobicity by varying the plasma exposure time. The Leidenfrost temperature for the smooth surface sphere changes gradually between the  $T_L$ -values for the hydrophilic and hydrophobic surface. As expected, the textured surface shows a much greater variation in  $T_L$ . For superhydrophilic spheres,  $T_L = 700 \text{ °C}$ , substantially higher than for the smooth hydrophilic surface where  $T_L = 254 \text{ °C}$ . For contact angles of about 50° - 70°, the textured surface  $T_L$  is close to the smooth surface  $T_L$ ; for textured surfaces of contact angle more than about 140° there was no transition to nucleate boiling. The contact angles are measured at room temperature.

In other series of superhydrophobic sphere-cooling experiments, we varied the initial sphere temperature. We confirmed that  $T_S$  vs.  $t$  data follow the same master curve for the initial sphere temperatures in 150 °C to 400 °C range.

An alternative superhydrophobic coating was produced using Cytronix PFC 1604V suspension liquid. The manufacturer's description of the product is "FluoroPel co-polymer solutions containing dispersions of superhydrophobic nano-particles" (<http://www.cytonix.com>). An SEM image of the coating is given in Fig. 1e and 1f. Application of this alternate agent to the steel spheres resulted in a translucent appearance surface layer and water contact angles of more than 160°. The spheres retained their hydrophobicity during heating to temperatures of about 300 °C. Fig. 8 compares the temperature-dependence of both Glaco and Cytonix coated spheres cooling in 80 °C and 100 °C water. The agreement between the data sets for the two coatings is excellent and confirms that a superhydrophobic coating with thermal properties discussed in our manuscript can be easily prepared using a range of readily available commercial products.

## 2 Experimental details for the heater device experiments

### 2.1 Immersion heater device and measurement protocol

The immersion heater device is shown schematically in Fig. 9a and a photograph of the setup in the laboratory is shown in Fig. 9b. The principal component is a hollow, stainless steel cylinder with a rounded tip (outer diameter of 24 mm, inner diameter of 16 mm, and total length of 72 mm), which was custom-made by TSE Troller AG, Switzerland. The outer surface of the cylinder is polished to a smooth finish (roughness  $R_a = 0.4 \mu\text{m}$ ). A 2.0 mm hole is drilled along the length of the cylinder wall to allow the insertion of thermocouple probe to measure the temperature at the cylinder wall close to the rounded tip (Fig. 9a). An electric heater element is fitted snugly inside the steel cylinder. The element

itself is a cartridge heater customized to operate at low-voltage to ensure safe operation of the device. The heating coil is made of 1 mm thick nickel-chromium alloy resistant wire (NI80-040-50, Omega Engineering) and has maximum operating power rating of about 250 W. The heater is powered by a programmable D.C. power supply (20V/50A VSP 2050, BK Precision) allowing precise output power control. We used the same K-type thermocouple probe as in the sphere-cooling experiments to monitor the cylinder surface temperature.

The immersion heater was operated in a Pyrex glass beaker filled with water and placed on a temperature-controlled hot plate (Fig. 9b). The experiments discussed here were conducted in water heated to saturation temperature, e.g.  $T_W = 100\text{ }^\circ\text{C}$ , by adjusting the hot plate power to maintain the water in the beaker at slow boiling. For most of the measurements the heater was warmed up to about  $100\text{ }^\circ\text{C}$  before immersion, after which the power on the heater was adjusted to the desired value by setting the voltage and recording the voltage and current values. The temperature was then monitored until it reached an equilibrium value for the set power, which typically took 5 to 15 minutes. For consistency the heater was always immersed to the same depth in the water beaker (about 40 mm). To compensate for water evaporation the water level was frequently re-adjusted to the initial level by pouring boiling water into the beaker. All temperature readings were taken at the set level of water and heater immersion depth. The heat flux average value was calculated as:

$$q[\text{W}/\text{cm}^2] = V[\text{V}]I[\text{A}]/S[\text{cm}^2] \quad (\text{S2})$$

where  $V$  and  $I$  are the set voltage and current values and  $S$  is the surface area of the heater immersed in the water.

The surface of the heater was modified to be superhydrophobic, hydrophobic, hydrophilic or superhydrophilic by applying the same procedure as for the sphere-cooling experiments.

## 2.2 Experiments with the superhydrophobic surface

When the superhydrophobic cylinder is heated to the same temperature as the water and immersed, we initially observed the characteristic silver mirror-like sheen appearance, discussed in the previous section on superhydrophobic spheres, indicating a Cassie state (Fig. 10a). By increasing the heater power a smooth transition to a fully-developed Leidenfrost regime can be observed. The development of the Leidenfrost layer is indicated by the appearance of waves moving up along the cylinder surface, which become progressively more pronounced as the cylinder temperature increases. This can be seen in the image series in Fig 10a-h. In essence, this is the inverse of the sphere cooling experiment (compare Supplementary Movie 4 and Movie 5).

Results for the heat flux vs. surface temperature are given in Fig. 11 where data were collected both by gradually increasing the heater power (from  $q = 2.0 \text{ W/cm}^2$  to  $8.0 \text{ W/cm}^2$ ) and by gradually decreasing the heating power (from  $q = 8.0 \text{ W/cm}^2$  to  $2.0 \text{ W/cm}^2$ ). There is no indication of any hysteresis between the heating-up and cooling-down data. We also repeated the experiments after the cylinder had been left immersed in the beaker overnight (24 hours). As a result the surface appearance can change slightly from the initial shiny state to a more matte look (compare Fig. 12a and 12b.), indicating that with time the state of the vapour layer on the surface can become different from the initial Cassie state. However, upon re-heating the surface to a slight overheat of  $102 - 107 \text{ }^\circ\text{C}$  results in the transition to the Leidenfrost state without the nucleate boiling phase. A transient vapor layer texture phase can be observed in this case (Fig. 12c). Once in the Leidenfrost regime (Fig 12d), we observe the same heat flux vs. surface temperature dependence as for the case of the freshly immersed surface (Fig. 11).

## 2.3 Experiments with superhydrophilic, hydrophilic and hydrophobic surfaces

For superhydrophilic, hydrophilic and hydrophobic surfaces immersed in water whose temperature is close to saturation, the heat transfer is in the nucleate boiling phase for the

entire range of heater applied power (maximum heat flux is lower than the critical heat flux, CHF). In all cases, the surface temperature rises much slower with increasing heater power when compared to the superhydrophobic surface (manuscript Fig. 4, for  $q = 8.0 \text{ W/cm}^2$ ,  $T_s = 108 \text{ }^\circ\text{C}$  for the hydrophilic surface and  $T_s = 240 \text{ }^\circ\text{C}$  for the superhydrophobic surface). Fig. 13 shows high-speed camera snapshots of the typical appearance of the superhydrophilic (Fig. 13a), hydrophilic (Fig. 13b) and hydrophobic (Fig. 13c) surface in the nucleate boiling regime.

We also conducted cooling experiments by immersing the cylinder after it has been heated to about  $400 \text{ }^\circ\text{C}$ . In such case the hydrophobic and hydrophilic surfaces are initially in the Leidenfrost state and they start to cool down in a similar manner to the spheres. If the heater power is maximized immediately after immersion, it is possible to sustain the hydrophobic surface in the Leidenfrost regime. For the case of the hydrophilic surface, however, the maximum applied power is not high enough to maintain the Leidenfrost regime and the vapour layer collapses when the surface temperature falls to about  $250 \text{ }^\circ\text{C}$ . While the hydrophobic surface heater is in the Leidenfrost regime it follows the same boiling curve as the superhydrophobic surface (manuscript Fig. 4). At temperatures below  $160 \text{ }^\circ\text{C}$  (Leidenfrost temperature) the layer collapses and the surface temperature bifurcates from the Leidenfrost branch to the nucleate boiling branch (see open green triangles in manuscript Fig. 4).

## 2.4 Steel cup container experiments.

To validate that the effect of hydrophobicity on the boiling transition is independent of the heater geometry, we performed experiments using a cylindrical stainless steel cup as shown in Fig. 14. The interior surface of the cup can be made hydrophobic or textured superhydrophobic by the same surface treatment as for the steel sphere and cylinder. The dimensions of the cup are: outer diameter of 40 mm, inner diameter of 30 mm, depth 40 mm and a bottom wall thickness of 8 mm. A 2 mm hole was drilled through the cup bottom

to allow placement of a thermocouple probe to measure the temperature of the bottom of the container (Fig. 14a). The cup is filled with water and heated on a temperature-controlled hot plate (Fig. 14b). Then we simply measure the dependence of the cup surface temperature (i.e. the thermocouple probe reading) as a function of the set temperature on the hot plate. As with the immersion heater experiments, we take an equilibrium surface temperature reading for each set value of the plate temperature and the water level in the cup was adjusted periodically to compensate for the evaporation, by pouring boiling water into the cup.

In Fig. 15 we compare data for the surface temperature vs. the plate set temperature (proportional to the heat flux) for hydrophilic and superhydrophobic cups. The data exhibit the same qualitative trend as for the immersion experiments, giving roughly the same magnitude of difference between the hydrophilic and the superhydrophobic surface (compare manuscript Fig. 4 and supplementary Fig. 15).

## 2.5 Leidenfrost droplet evaporation experiments

We repeat the original 1756 Leidenfrost experiment to measure the evaporation of small water droplets on hot hydrophobic or textured superhydrophobic surfaces. We use the same steel cup container experimental set-up described in the previous section (Fig. 14) to measure the time for evaporation of small water droplets as a function of surface temperature.

In this experiment the steel cup is kept empty. The container surface temperature, registered by the thermocouple probe, is set by regulating the hot plate temperature. Using a micropipette, a water droplet is carefully deposited on the container bottom and the time for the complete evaporation of the droplet at a given surface temperature is measured. In all experiments the initial volume of the deposited droplet is 100  $\mu\text{l}$ , corresponding to a 5.76 mm diameter spherical droplet. One side of the hot plate was slightly elevated to give a small tilt of several degrees to the container bottom surface. The tilt makes the droplet on a

superhydrophobic surface as well as droplets in Leidenfrost regime slide to the side wall of the container to limit the spontaneous motion of the droplet around the container bottom that would otherwise give rise to random variations of the droplet evaporation time (see photograph in Fig. 14c).

In Fig. 16 we compare the data for the droplet evaporation time vs. surface temperature for hydrophobic and textured superhydrophobic container surfaces. The data for the hydrophobic surface follow the classical dependence observed in this type of experiments<sup>2,3</sup>. From just above 100 °C, the evaporation time decreases rapidly with increasing temperature as heat transfer occurs in the nucleate boiling regime. Indeed, in the temperature range 120 °C - 150 °C mini-bubbles can be observed nucleating in the droplet-surface contact zone. The evaporation time exhibits a minimum around 140 °C. On reaching the Leidenfrost point temperature,  $T_L = 160$  °C, heat transfer enters the Leidenfrost film-boiling regime and the droplet is levitated by the insulating vapour layer giving rise to a sharp increase of the evaporation time (Fig. 16). Further increases in the surface temperature result in a slow decrease of the evaporation time as expected in Leidenfrost regime. At temperatures below  $T_L$ , the droplet makes a contact angle of  $\sim 100^\circ$  with the hydrophobic surface, similar to that in Fig. 2c. However, above  $T_L$  the droplet assumes a near spherical shape, similar to that of a droplet deposited on a superhydrophobic surface at room temperature shown in Fig. 2a.

In contrast, the droplet evaporation time on heated superhydrophobic surfaces decreases monotonically with increasing temperature between 100 °C and 160 °C without exhibiting a minimum (Fig. 16). For surface temperatures above 160 °C, the evaporation times as well as droplet shapes on hydrophobic and superhydrophobic surfaces are identical within experimental error. This can be taken as evidence that heat transfer above 160 °C takes place in the film boiling Leidenfrost mode on both types of surfaces. However, at temperatures between 100°C - 160°C, the evaporating drops on heated superhydrophobic surfaces appear spherical (similar to that in Fig. 2a) and are highly mobile along the surface

as might be expected for droplets in the classical Leidenfrost regime. Furthermore, no mini-bubbles are observed around the droplet-surface contact zone at the superhydrophobic surface at any temperature.

Therefore, we infer from the above observations that at all superheats surface temperatures above 100 °C the evaporating droplet at superhydrophobic surfaces, is always supported by a vapour layer. As a result, heat transfer at superhydrophobic surfaces always occurs in the film-boiling mode as there is no evidence that nucleate boiling occurs. The results for the single droplet evaporation experiments are in complete agreement with the pool-boiling experiments discussed in this paper. The above conclusions are also in accord with the observed silver-mirror sheen of a submerged superhydrophobic surface (Fig. 1c in the manuscript) that is indicative of a Cassie state vapour film that exists at the water-superhydrophobic surface even at room temperatures.

### **3 Stabilisation of the vapour phase due to surface texture**

The presence of a vapour film adjacent to a heated surface is a consequence of a dynamic heat transfer and fluid flow condition. When there is a vapour film present, the liquid-vapour interface can have perturbations. Consequently, the perturbed interface may touch the solid. If the wetting of the solid surface and disruption of the vapour film are energetically favorable compared to the film-wise state then the vapour film collapses<sup>3</sup>. This is consistent with observations in the superhydrophilic, hydrophilic and hydrophobic sphere cases, where a rapid collapse of the vapour film to a nucleate boiling mode is observed. However, such a transition is not observed for the superhydrophobic case where the surface texture plays an important role. This is discussed below.

In the “Glaco coating” textured superhydrophobic surface case, the smallest roughness scale is nanoparticles that are 50 nm in diameter (Fig. 1a, c). The self-assembled

nanoparticles form a fractal-type structure with a coarse scale pillar-type roughness ranging from 0.1-2 micron spacing and 50-300 nm depth (Fig. 1a, b, c).

As shown in Fig. 17 we propose that, for a superhydrophobic surface, the vapour-film transitions to a Cassie state without passing through the nucleate boiling mode. If this hypothesis is true then, in the Cassie state, the liquid should not impale the roughness grooves that are occupied by the vapour. This is possible if it is energetically more favorable for the vapour to occupy the roughness grooves compared to the liquid impaling and wetting the rough surface. While the impalement is a dynamic process, simple estimates of the stability of the vapour in the roughness grooves can be made based on static equilibrium analysis<sup>5,6</sup>. In the following we will make such estimates about whether the vapour can be sustained in the roughness grooves at different conditions. In section 3.1 we consider the vapour sustainability in nanoscale scale roughness at ambient conditions (1 atm and 25 °C) and in section 3.2 we consider the vapour sustainability at the course scale roughness, but at saturation conditions for both the liquid and the vapour phase.

### 3.1 Nanoparticle scale roughness

For the Glaco coating the nanoparticles in the superhydrophobic coating are estimated to be 50 nm in diameter. Thus, the smallest pore sizes between self-assembled nanoparticles that are touching one-another would be of similar order at the very least. For the purposes of calculations let the pore diameter be 50-100 nm. For simplicity, assume cylindrical pores (actual geometry will have a re-entrant type shape which will further resist impalement of the liquid into the grooves). Since, it is observed in our experiments that the vapour continues to exist even when the superhydrophobic sphere is completely cooled to a temperature of the ambient water, we enquire if it is possible for the vapour to exist in the pores without the liquid impaling it even at ambient conditions (1 atm and 25 °C).

To answer the issue above, we perform equilibrium thermodynamic analysis.<sup>5,6</sup> Consider a stable liquid at ambient condition above a cylindrical pore (Fig. 18). A liquid-vapour interface can hang at the top of the pore and the metastable vapour of that liquid can exist in the pore if the following conditions are satisfied (assuming temperature is uniform under fully cooled conditions):<sup>5,6</sup>

**i)** The liquid and the metastable vapour inside the pore are in chemical equilibrium. As shown in Fig. 18, the pressures of liquid A in chemical equilibrium with vapour B are unequal. For water at standard ambient atmospheric conditions we have  $T = 298$  K,  $p_A = 1$  atm (101.3 kPa),  $p_B \approx p_{sat} = p_C = 3.17$  kPa. Note that the vapour pressure at B is close to the saturation pressure at C.

**ii)** The liquid-vapour interface has a radius of curvature that balances the pressure difference across it. The radius of curvature  $R_{co}$  of this interface is given by the Young-Laplace equation:

$$R_{co} = 2\sigma_{lv}/(p_A - p_B) \quad (\text{S3})$$

where  $\sigma_{lv}$  is the liquid–vapour surface tension (assumed constant for simplicity). Using  $\sigma_{lv} = 72$  mN/m for water and the equilibrium pressure difference between the liquid and vapour phases at ambient conditions, discussed above, we get  $R_{co} = 1.47$   $\mu\text{m}$ .

**iii)** The liquid-vapour interface should hang at the top of the pore and satisfy the local contact angle at the corner. This is possible if the cylindrical pore diameter  $D$  satisfies the following condition:<sup>5</sup>

$$\frac{D}{R_{co}} < -2 \cos \theta_c \quad (\text{S4})$$

where  $\theta_c$  is the material contact angle. Assuming  $\theta_c = 100^\circ$  for the silanized nanoparticles, Eqn. (S4) implies that  $D < 510$  nm. Pores formed between 50 nm diameter nanoparticles easily satisfy this condition.

Thus, the above analysis shows that metastable vapour pockets can be sustained in pores between 50 nm diameter spheres even at room conditions. In addition, these pores will provide active nucleation sites during superheated conditions<sup>5</sup>.

### 3.2 Coarse scale roughness

Two levels of coarse scale roughness of the Glaco coating are shown in Fig 1a-c for the fractal type geometry of the self-assembled nanoparticles. The coarse scale is pyramidal pillar type (Fig. 19). The surface of the pillars is made from nanoparticles and is not smooth.

As the vapour-film relaxes to a Cassie state without transitioning to the nucleate boiling mode the liquid-vapour interface should be able to hang between peaks on the coarse scale roughness (Fig. 17 and Fig. 19). Impalement of the liquid into the roughness grooves should not occur. During boiling under superheated condition the vapour pressure is typically greater than that of the fluid (Fig. 18). Thus, the liquid-vapor interface would be curved out of the roughness groove. If instead, one assumes saturated condition of both the liquid and the vapor at the liquid-vapor interface during boiling, then the interface will be flat. The condition for this flat interface to hang between pillar tops is the more restrictive case of the two configurations. We will therefore scrutinize the flat interface to ensure that the liquid does not impale the roughness grooves to cause a complete vapor layer collapse.

The AFM image in Fig. 1a shows pyramidal roughness structures with spacing between peaks ranging from 100-200 nm and depths ranging from 50-200 nm. This surface can be approximated by pyramidal pile of nanoparticles with a surface inclined an angle  $\alpha$  of 26°-76°. Fig. 1b shows pyramidal larger-scale roughness with spacing between peaks ranging from 1-2  $\mu\text{m}$  and depths ranging from 200-300 nm. This indicates an angle  $\alpha$  of 11°-31°.

Fig. 19a shows schematically a flat liquid-vapour interface hanging between pyramid tops. The liquid contact line can remain pinned on the apex of the top nanoparticle if the flat liquid surface does not touch the tip of the adjacent nanoparticle, as sketched in Fig. 19b. If the liquid surface touches the adjacent particle the liquid can climb down along the pillar, from one particle to the next, thereby filling the large-scale pore. How far the contact line moves down the side of the spherical shape depends on the local contact angle,  $\theta_c$ . For silanized nanoparticles the equilibrium  $\theta_c$  is about  $100^\circ$  or up to  $115^\circ$  if the advancing contact angle is considered (Fig. 2c). From the simplified geometry in Fig. 19b we see that  $\beta = \theta_c - 90^\circ$  and the contact line reaches to  $\theta_c$  above the equator. For nanoparticle of radius  $R$ , the liquid will touch the adjacent particle if  $R(1 - \sin \beta) = 2R \tan \alpha$ . This gives a critical relationship between pyramid and contact angles, i.e.  $\alpha = \arctan(0.5[1 - \sin(\theta_c - 90^\circ)])$  which is independent of  $R$ . For the equilibrium contact angle value of  $\theta_c = 100^\circ$  we get the condition that for the liquid-vapour interface to be pinned near the pillar top  $\alpha > 23^\circ$ , and if the advancing contact angle  $\theta_c = 115^\circ$  is considered  $\alpha > 16^\circ$ . As seen above, the value of  $\alpha$  ranges between  $11^\circ$ - $76^\circ$ . It is thus clear that a large majority of the coarse scale pyramidal pillars satisfy the condition for a flat liquid-vapor interface to be pinned between pillar tops.

As the system cools to sub-cooled conditions the liquid-vapor interface may eventually impale the coarse scale roughness. However, as shown earlier, the pores between the nanoparticles are small enough that the metastable vapour will still be sustained in those pores.

## References:

1. Zvirin, Y., Hewitt G. R. & Kenning, D. B. R. Boiling on free-falling spheres: Drag and heat transfer coefficients. *Exp. Heat Transfer* **3**, 185-214 (1990).
2. Biance, A. L., Clanet C. & Quere, D. Leidenfrost drops. *Phys. Fluids* **15**, 1632-1637 (2003).
3. Kim, H., Truong, B., Buongiorno, J. & Hu, L. On the effect of surface roughness height, wettability, and nanoporosity on Leidenfrost phenomena. *App. Phys. Letts.* **98**, 083121 (2011).
4. Carey, V. P. *Liquid-vapor phase-change phenomena* 2<sup>nd</sup> Edition, Taylor and Francis, 2008.
5. Patankar, N. A. Supernucleating surfaces for nucleate boiling and dropwise condensation heat transfer. *Soft Matter* **6**, 1613-1620 (2010).
6. Patankar, N. A. Vapor stabilizing substrates for superhydrophobicity and superslip. *Langmuir* **26**, 8783-8786 (2010).

## Supplementary Movie Legends:

**Supplementary Movie 1.** Cooling of a 20 mm diameter hydrophilic sphere in 22 °C water. The initial temperature of the sphere is about  $T_S = 600$  °C and the explosive transition occurs at about  $T_S = 400$  °C. The frame rate used was 25 fps with shutter speed set at 1/1000 sec, video playback speed is 30 fps.

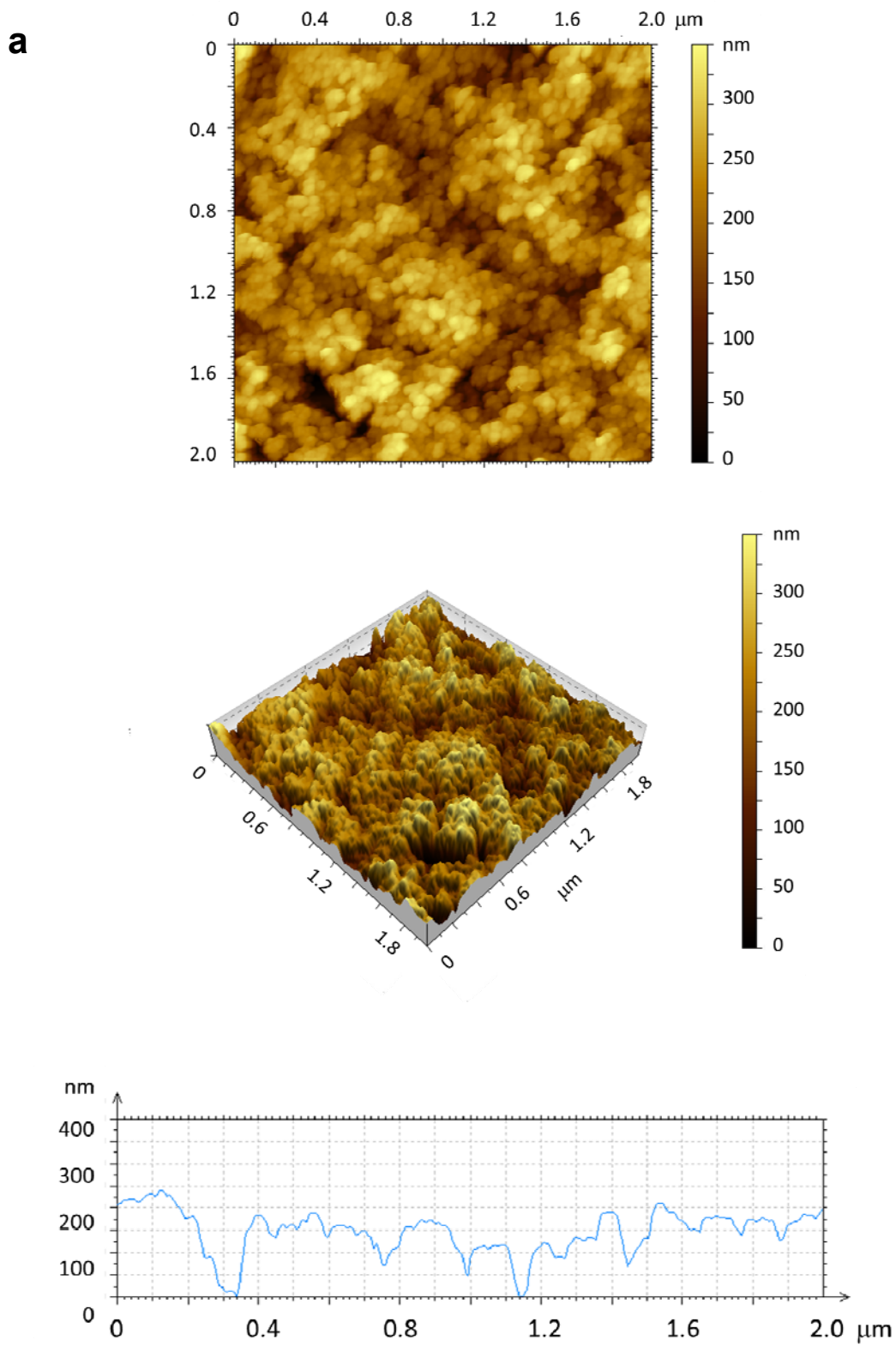
**Supplementary Movie 2.** Cooling of a 20 mm diameter hydrophobic surface steel sphere in 22 °C water. The initial temperature of the sphere is about  $T_S = 350$  °C and the explosive transition occurs at about  $T_S = 200$  °C. The frame rate used was 25 fps with shutter speed set at 1/1000 sec, video playback speed is 30 fps.

**Supplementary Movie 3.** Cooling of a 20 mm diameter superhydrophobic surface steel sphere in 22 °C water. The initial temperature of the sphere is about  $T_S = 380$  °C. The frame rate used was 25 fps with shutter speed set at 1/1000 sec, video playback speed is 30 fps.

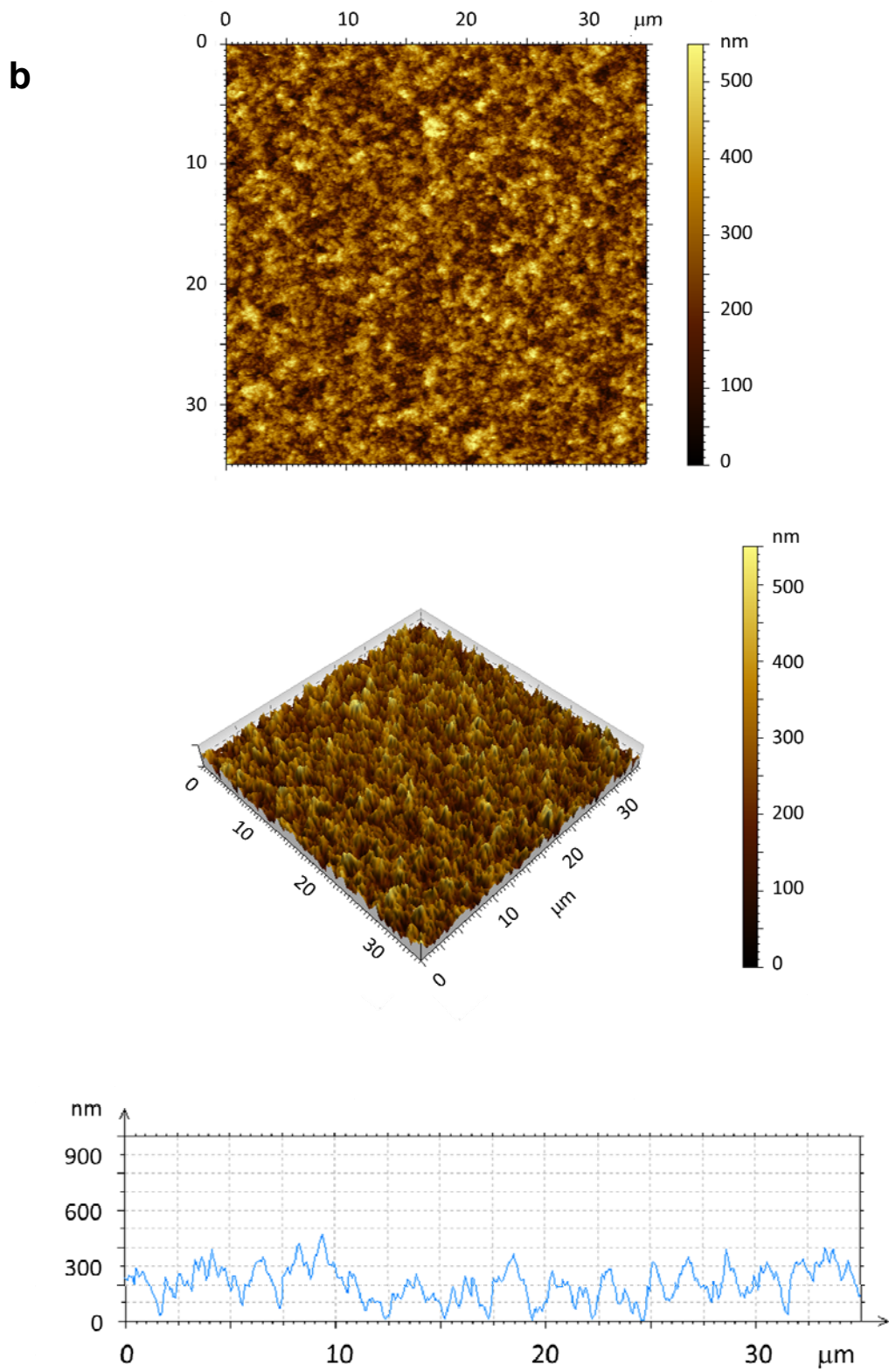
**Supplementary Movie 4.** Combined movie showing the cooling of 20 mm hydrophilic (left side) and superhydrophobic (right side) steel sphere in 100 °C water. The spheres initial temperature is about  $T_S = 380$  °C. The frame rate used is 5 fps with shutter speed set at 1/500 sec, video playback is 30 fps.

**Supplementary Movie 5.** Combined movie showing steel cylinder heater with a superhydrophobic surface immersed in 100 °C water. The cylinder surface temperature is  $T_S = 100$  °C (left side),  $T_S = 107$  °C (middle) and  $T_S = 200$  °C (right). The frame rate used is 50 fps with shutter speed set at 1/1000 sec, video playback is 30 fps.

### Supplementary Figures and Legends

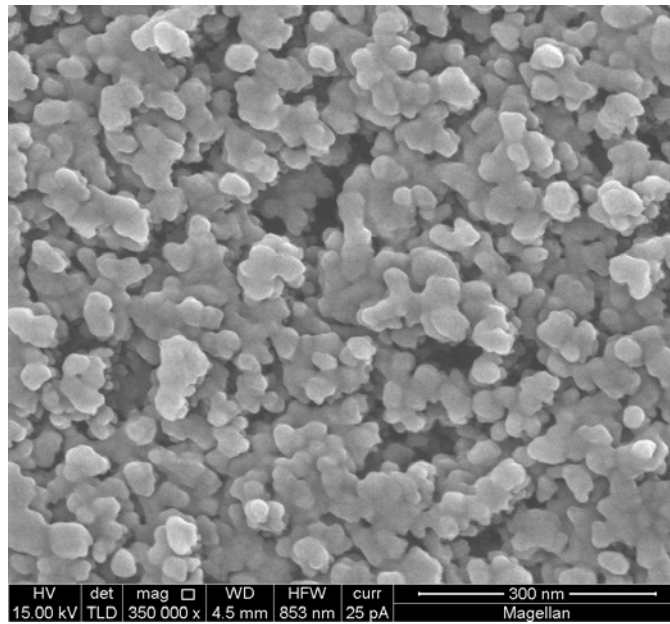


Supplementary Figure 1a.

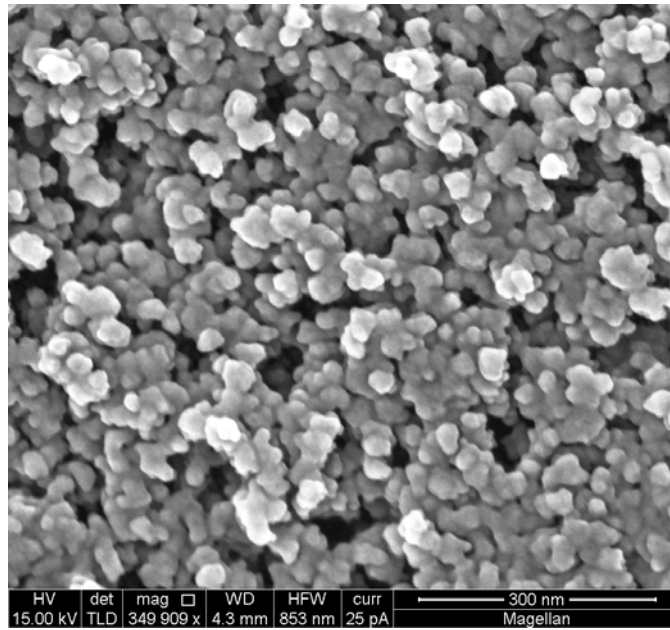


Supplementary Figure 1b.

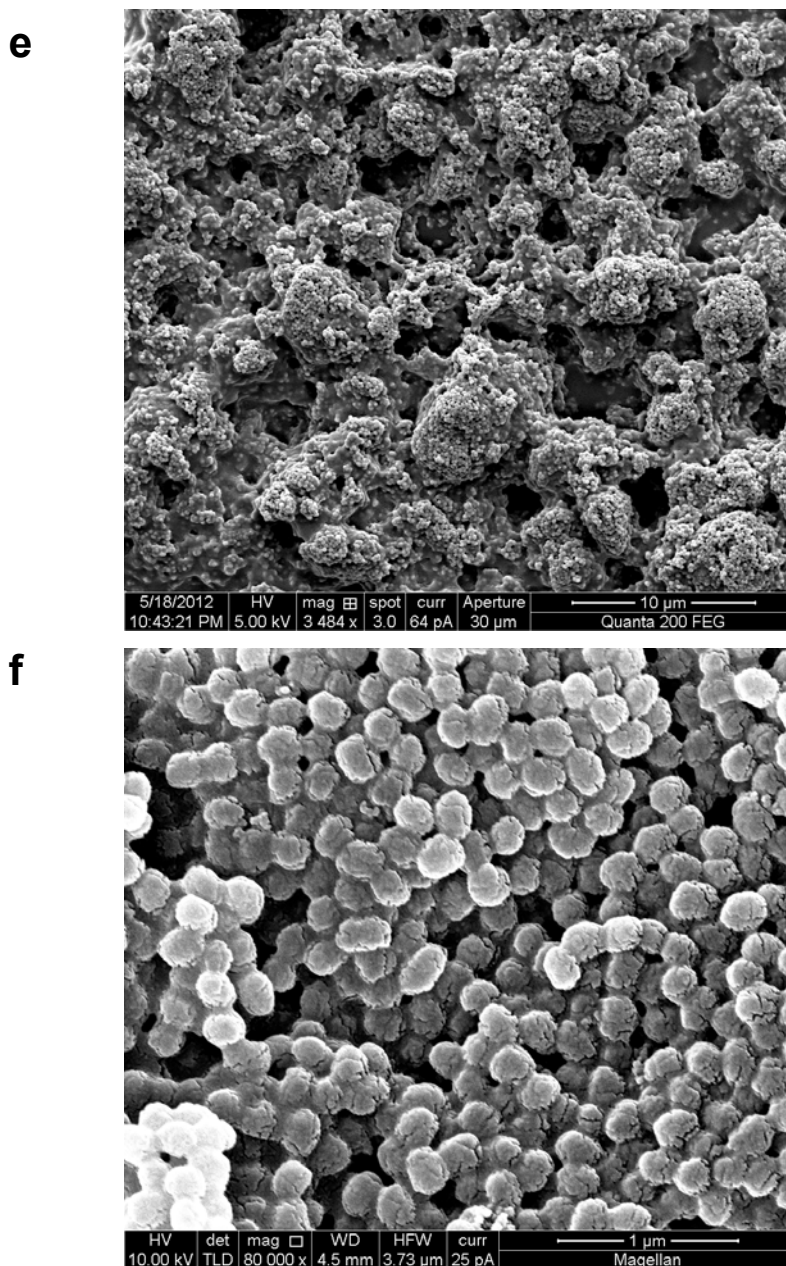
**c**



**d**

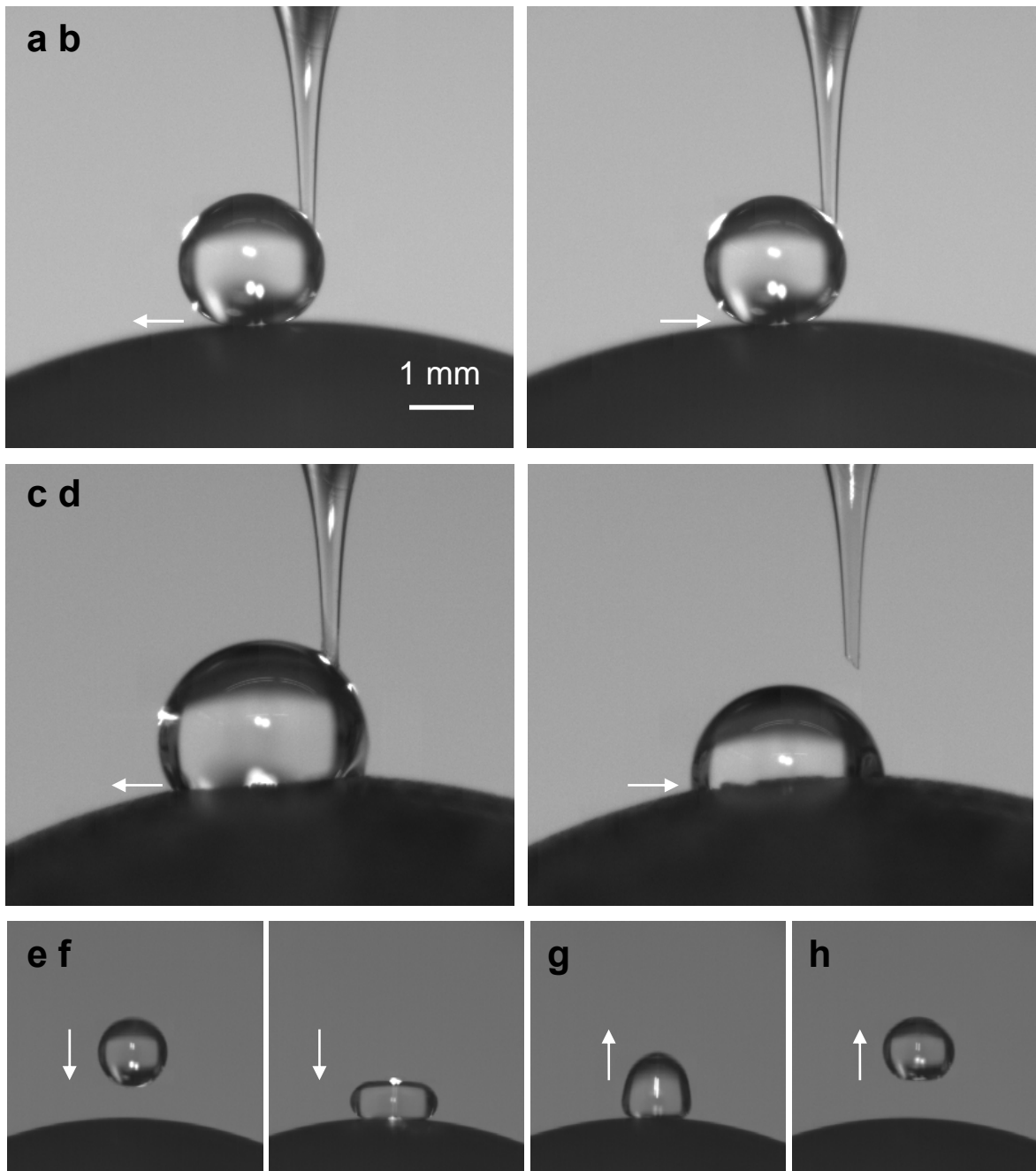


**Supplementary Figure 1c and 1d.**



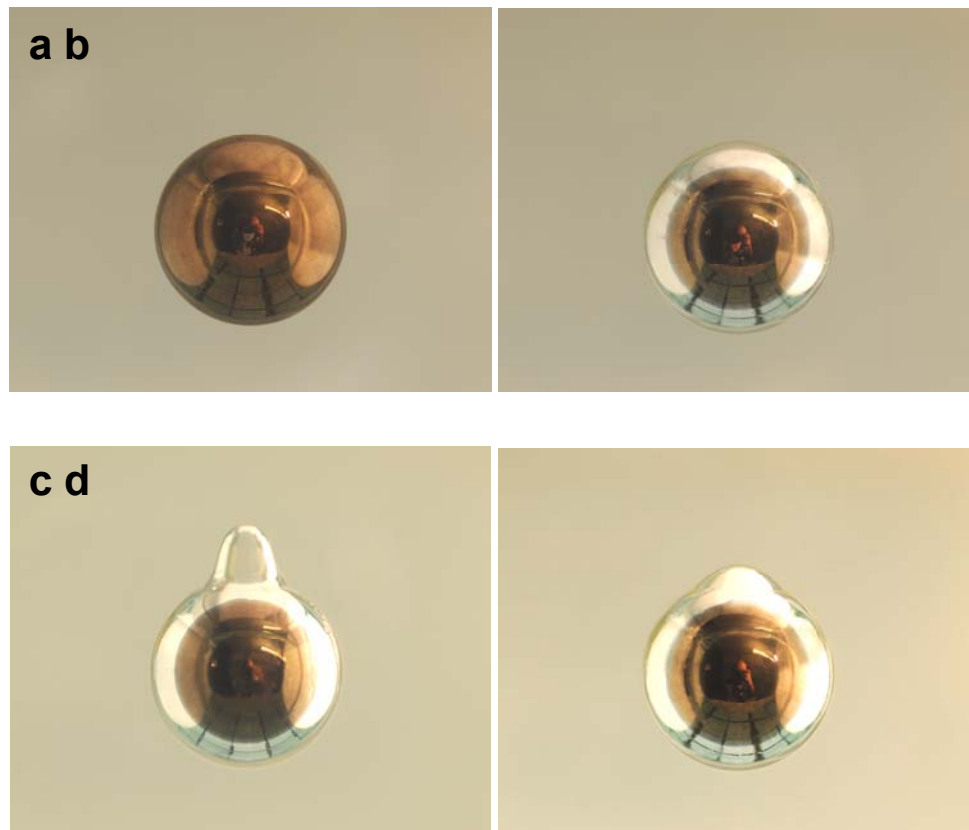
**Supplementary Figure 1. AFM and SEM images of the superhydrophobic coatings.**

AFM topographic images (a)  $2\ \mu\text{m}^2$  and (b)  $35\ \mu\text{m}^2$  surface of the “Glaco mirror coat Zero” coating deposited on a plain silicon wafer. Shown for each are plain and 3D views together with a cross-section profile. SEM image of the same “Glaco” coating before (c) and after (d) plasma treatment that alters the surface from being superhydrophobic to superhydrophilic. (e) and (f) are SEM images of Cytronix PFC 1604V coating deposited on a silicon wafer.



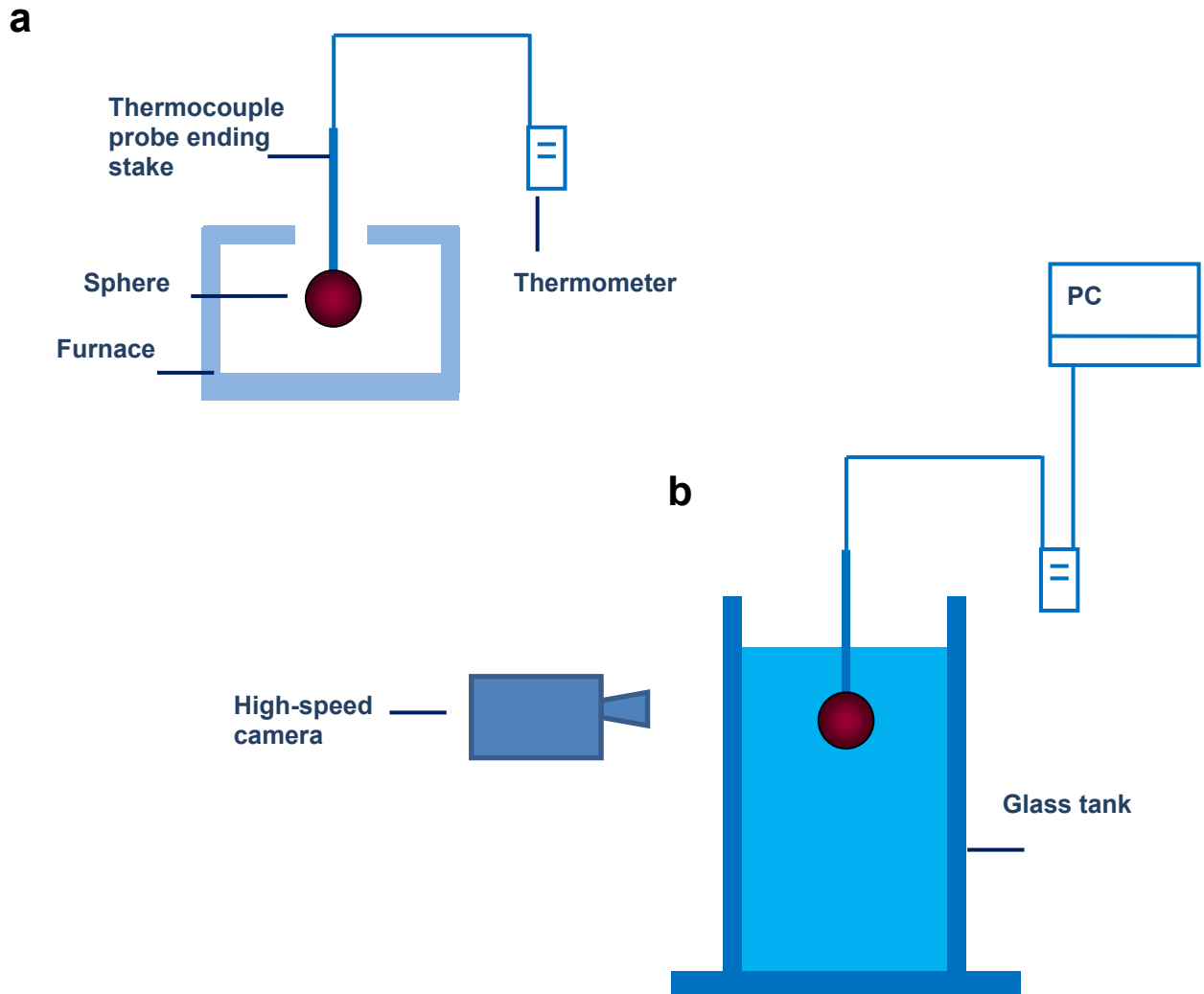
### Supplementary Figure 2. Contact angles estimation.

High-speed camera images of a water droplet pressed against a superhydrophobic surface sphere during the droplet advancing (a) and receding (b), or against a hydrophobic surface sphere during the droplet advancing (c) and after the droplet receding (d). (e)-(f) show the impact-rebound sequence of a water drop released from a few cm above a superhydrophobic sphere.



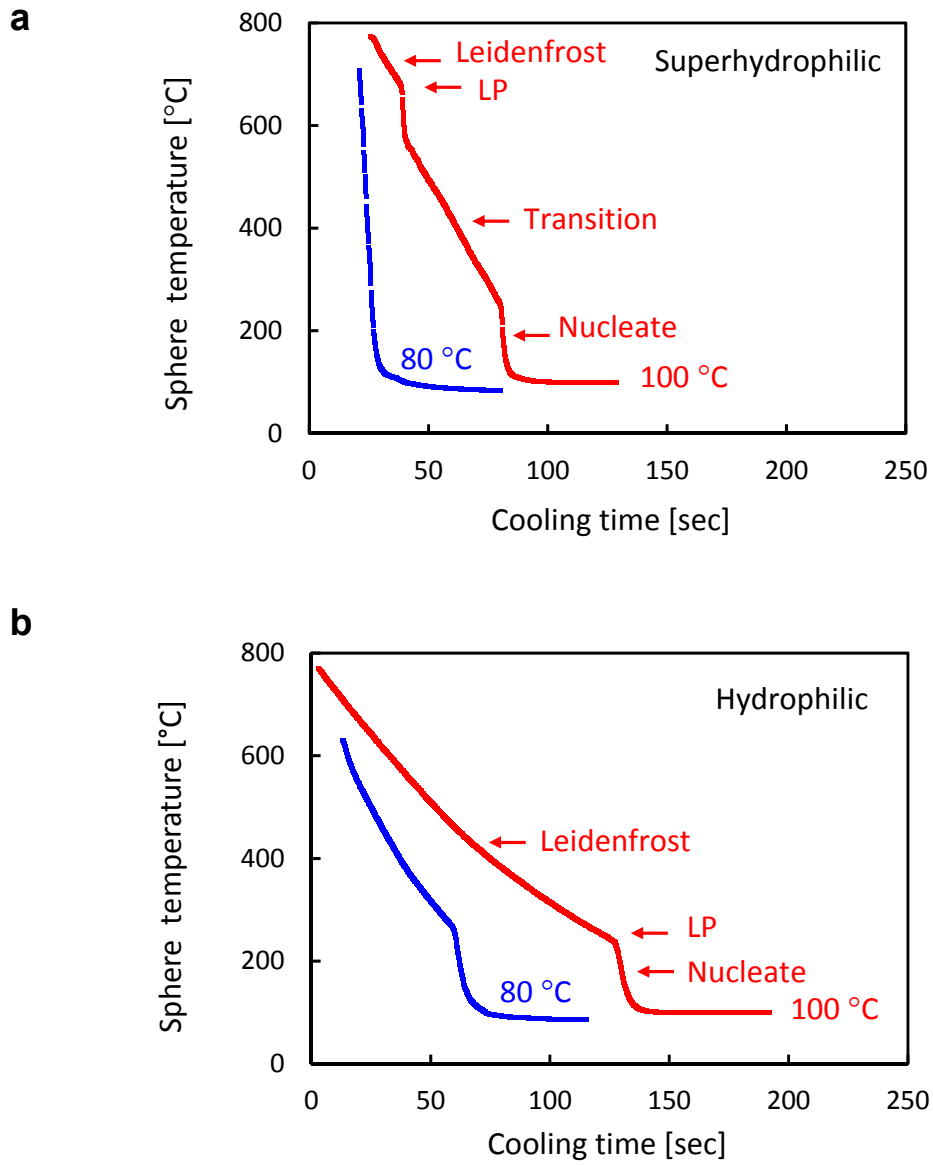
**Supplementary Figure 3. Image of immersed spheres.**

Digital camera images of a 20 mm steel sphere immersed in water: (a) hydrophilic sphere immersed in room temperature water; (b) superhydrophobic sphere immerse in room temperature water (both spheres also at room temperature); (c) heated superhydrophobic sphere cooling in 22 °C water during the Leidenfrost regime,  $T_s = 350$  °C (c); and after cooling to the pool temperature,  $T_s = 22$  °C.



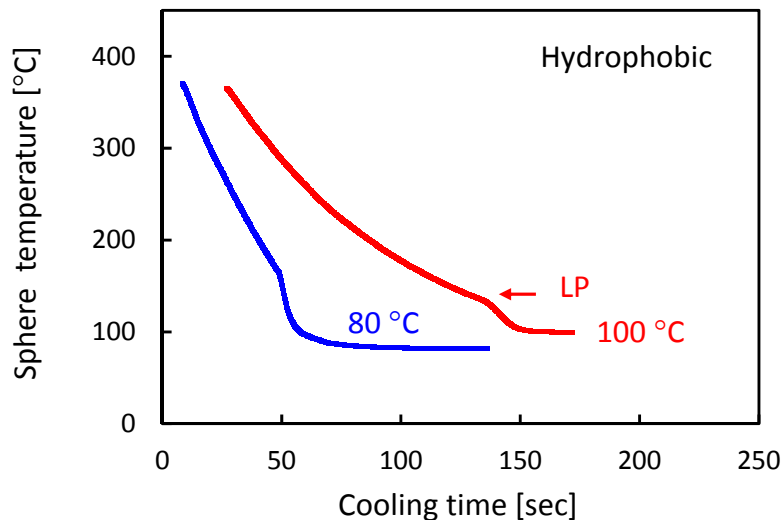
**Supplementary Figure 4. Experimental set-up.**

Schematic of the experimental set-up for the sphere probe heating (a) and cooling in water (b).

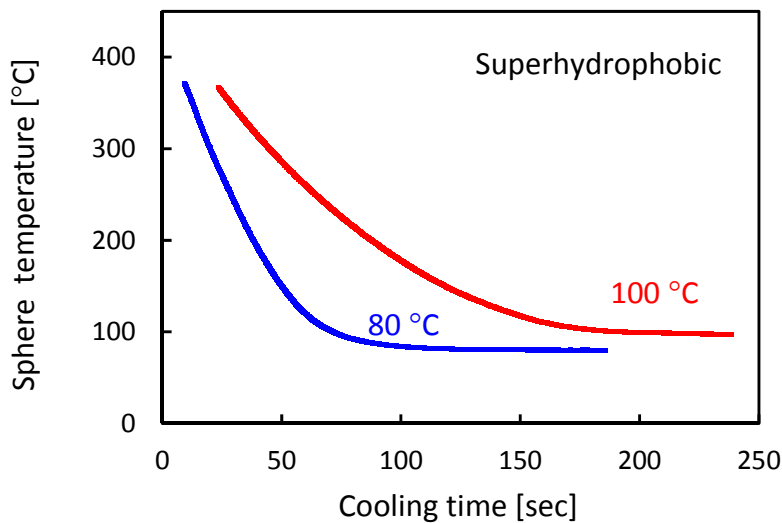


Supplementary Figure 5a and 5b.

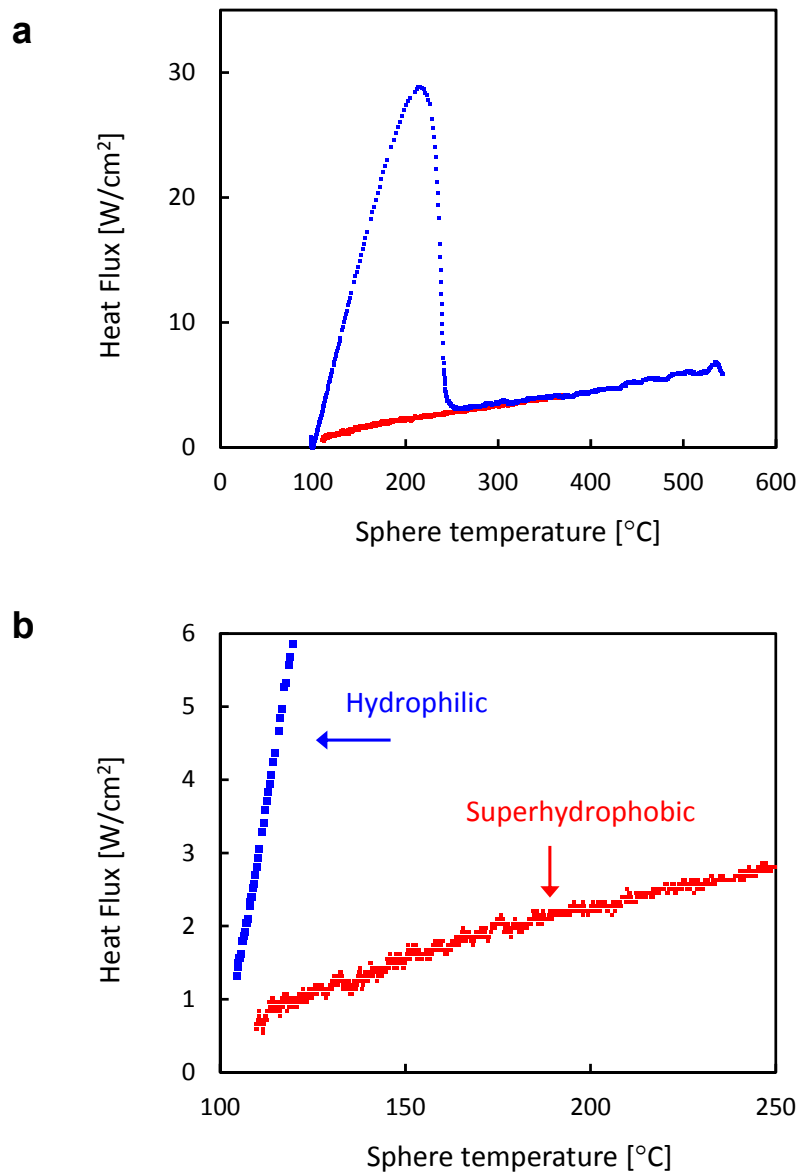
c



d

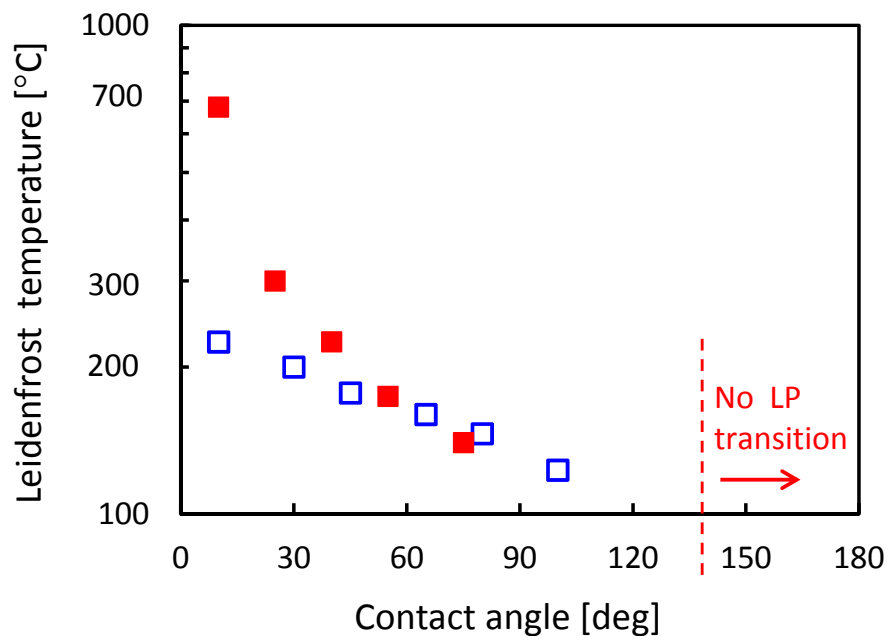
**Supplementary Figure 5. Sphere temperature vs. cooling time.**

Sphere temperature vs. cooling time for 20 mm steel sphere cooling in a 80 °C water (blue line) or 100 °C water (red line): (a) superhydrophilic, (b) hydrophilic, (c) hydrophobic and (d) superhydrophobic sphere.



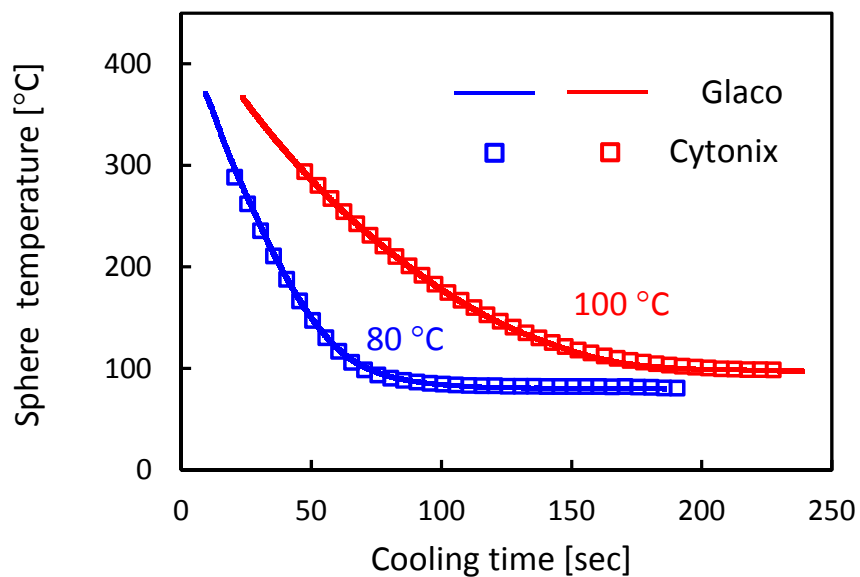
### Supplementary Figure 6. Heat flux vs. sphere temperature.

Instantaneous heat flux vs. sphere temperature for sphere cooling in 100 °C water. Hydrophilic sphere results (blue line) are calculated from temperature vs. time data presented in Fig. 5b and superhydrophobic sphere results are calculated from the data presented in Fig. 5c (red line), (b) shows the zoomed-in region of (a) in the low-heat flux range data.



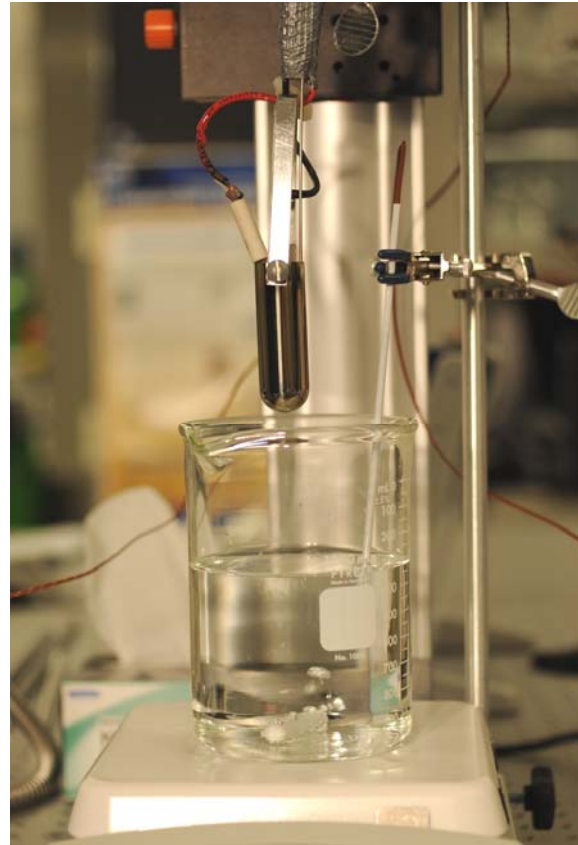
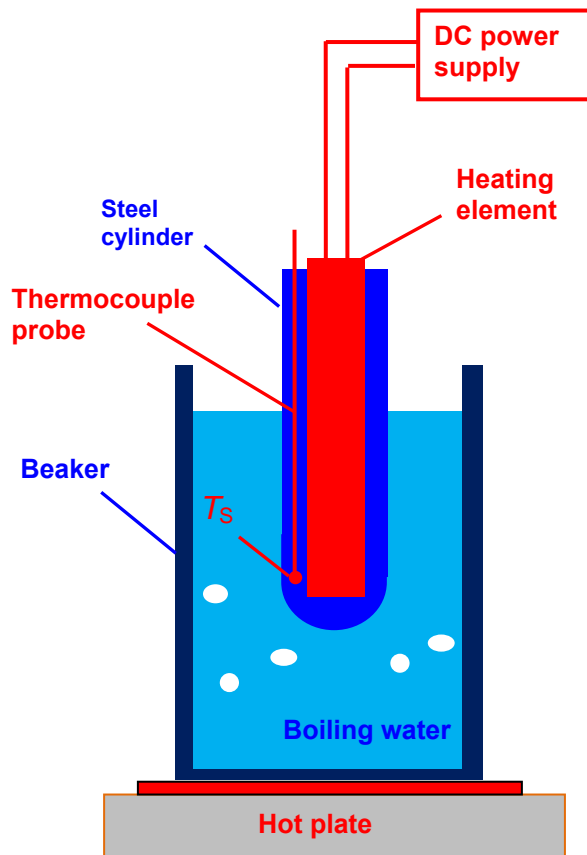
**Supplementary Figure 7. Contact angle vs. Leidenfrost temperature.**

Leidenfrost transition temperature (logarithmic scale) as a function of the contact angle at room temperature for smooth surface (open blue) and textured Glaco-coated surface (solid red) 20 mm stainless steel spheres cooling in water at 100 °C. The left-most data points of about 10° correspond to the hydrophilic sphere (open blue) and superhydrophilic sphere case (solid red). The  $T_S$  vs.  $t$  dependence for Glaco-coated spheres with contact angles of more than 140° does not exhibit a Leidenfrost transition.



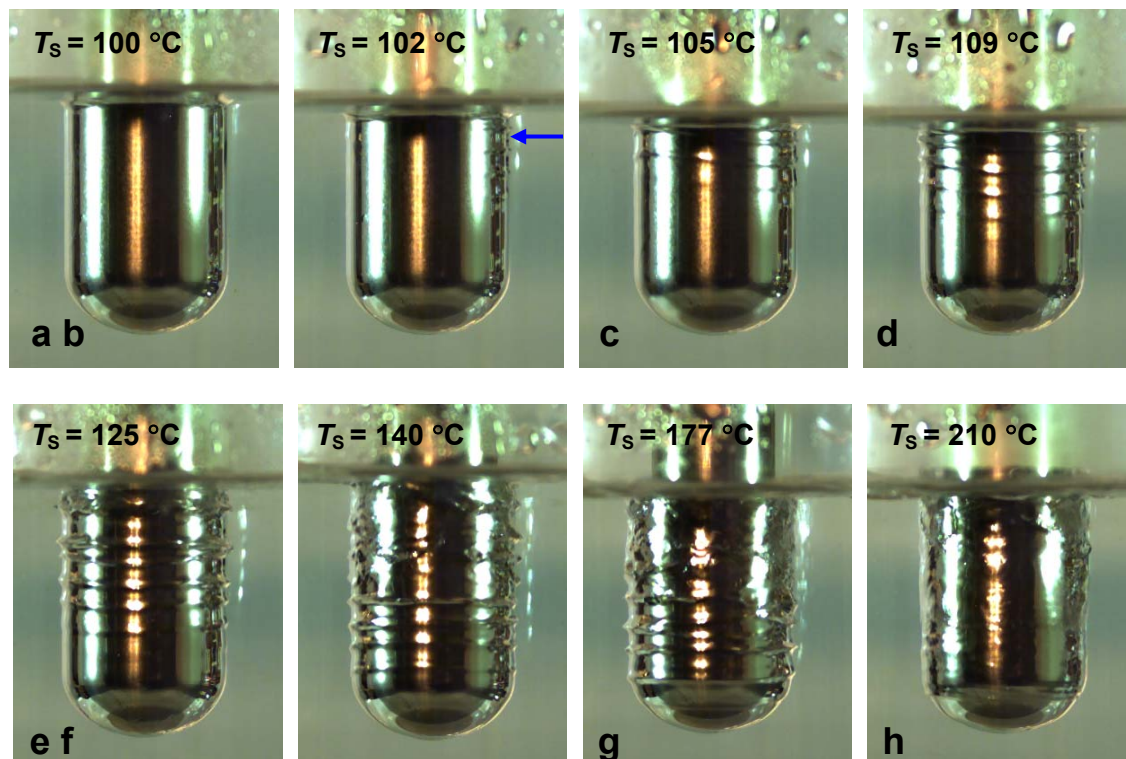
**Supplementary Figure 8. Glaco and Cytonix coatings.**

Sphere temperature vs. cooling time for 20 mm steel sphere coated with Glaco (solid lines) or Cytonix (open squares) superhydrophobic coating cooling in 80°C water (blue) or 100°C water (red).

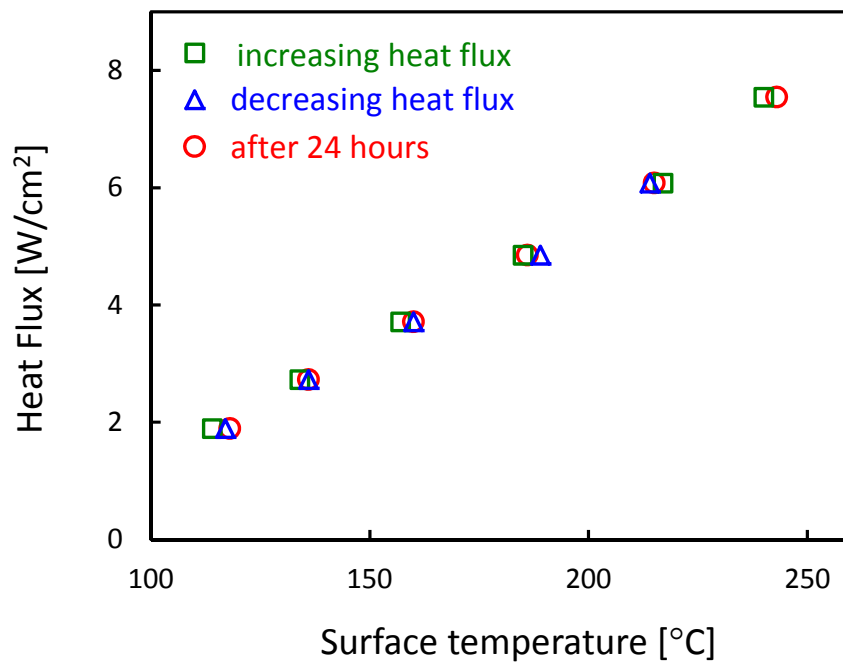


**Supplementary Figure 9. Immersion heater experimental set-up.**

(a) Detailed schematic and (b) photograph of the immersion heater device and experimental set-up.

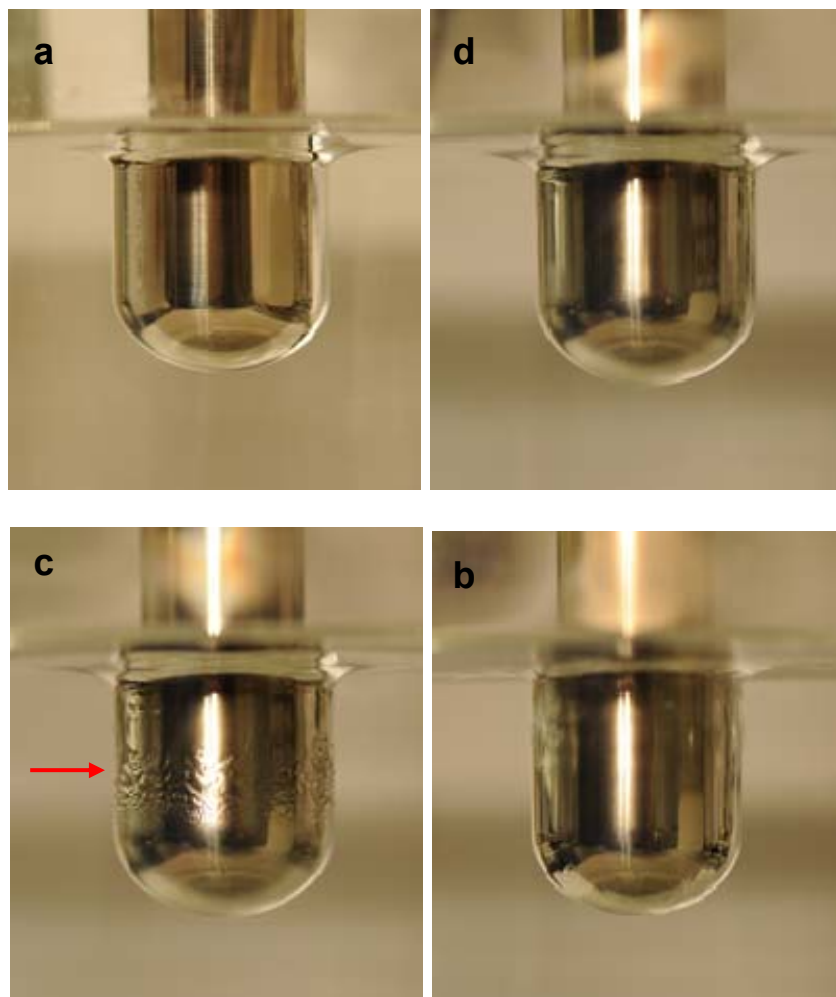


**Supplementary Figure 10. Snapshots of the heated superhydrophobic surface cylinder.** Snapshots taken from high-speed video sequences of the immersed cylinder with a superhydrophobic surface. The water is at  $100\text{ °C}$  and the surface temperature of the cylinder is indicated in the images. The blue arrow in (b) indicates the first manifestation of the Leidenfrost regime, in the form of small waves. See also Supplementary Movie 5.



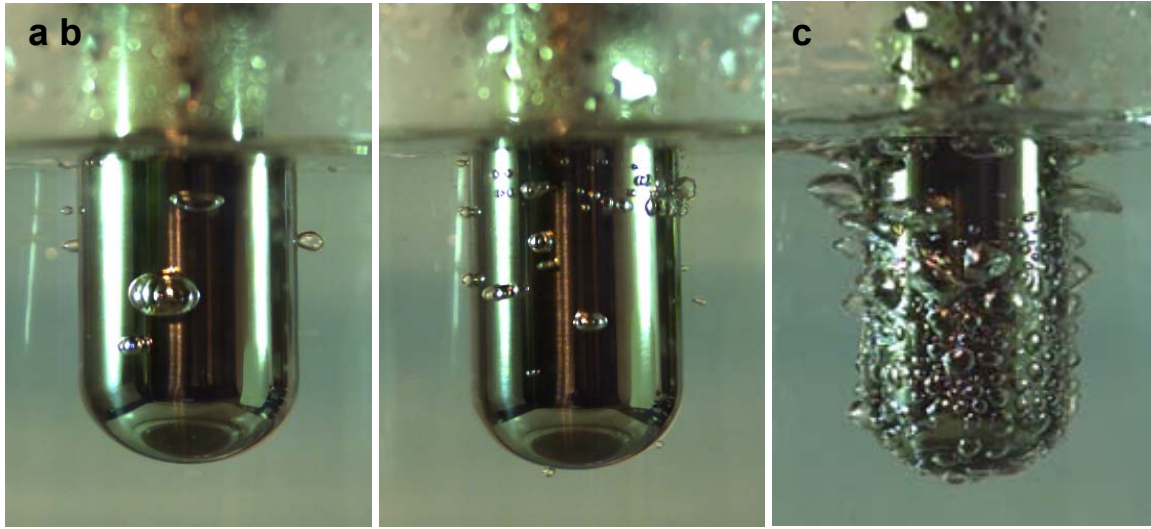
**Supplementary Figure 11. Heat flux vs. surface temperature.**

Dependence of the surface temperature on the heat flux for a superhydrophobic surface heater for both increasing heat flux (open square, green) and decreasing heat flux (open triangles, blue) mode. Measurements taken after the heater had been immersed for 24 hours are also shown (open circles, red).



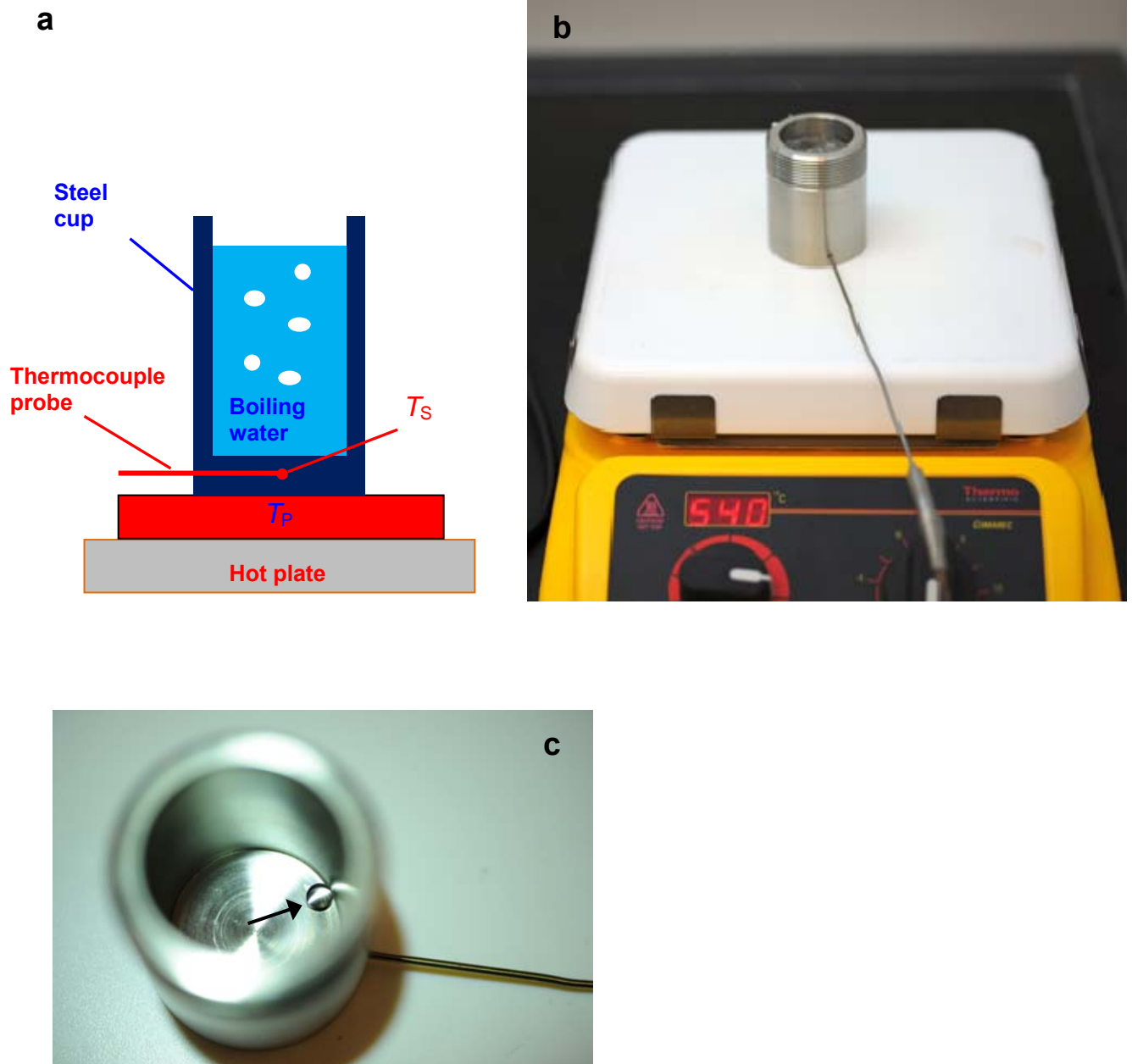
**Supplementary Figure 12. Images of the immersed superhydrophobic cylinder.**

Digital camera images of the superhydrophobic cylinder freshly immersed in room-temperature water (a) and after 24 hours (b). Images (c) and (d) are in boiling water conditions after the heater power has been increased to start overheating the surface. In (c) the surface temperature is about 105 °C and in (d) about 109 °C. A transitional texture vapour state can be observed in (c) indicated by the red arrow, whilst in (d) the entire surface of the heater is in Leidenfrost state.



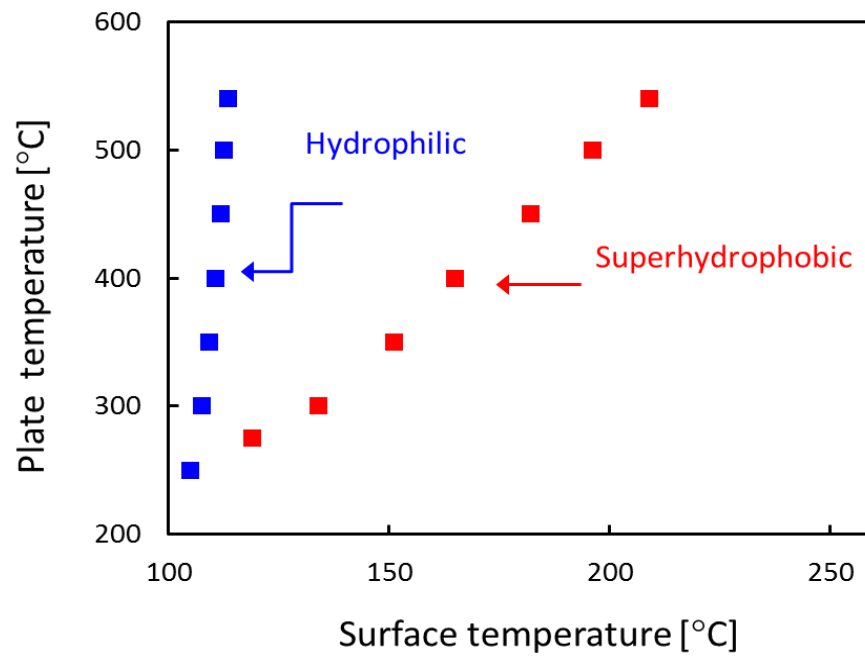
**Supplementary Figure 13. High-speed camera snapshots of the immersed cylinder.**

Snapshots of the immersed cylinder for (a) superhydrophilic, (b) hydrophilic and (c) hydrophobic surfaces. All images show varying degrees of nucleate boiling at surfaces temperatures of about 108 °C.



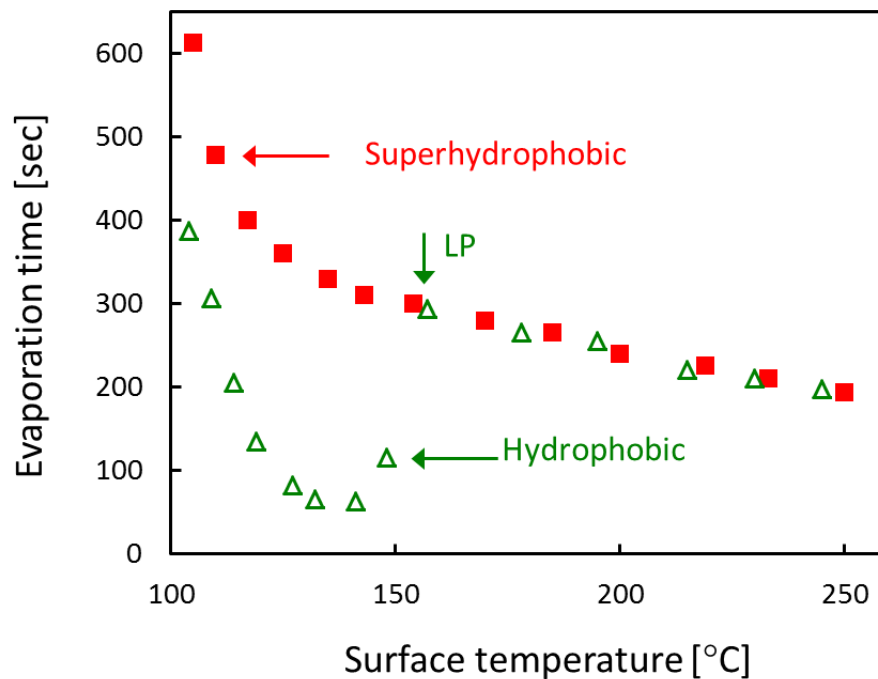
**Supplementary Figure 14. Steel cup experimental set-up.**

Detailed schematic (a) and photograph (b) of the steel cup vessel experimental set-up showing the thermal couple temperature probe at the bottom of the cup. (c) Top view of the steel cup with a water droplet at the bottom indicated by the arrow.



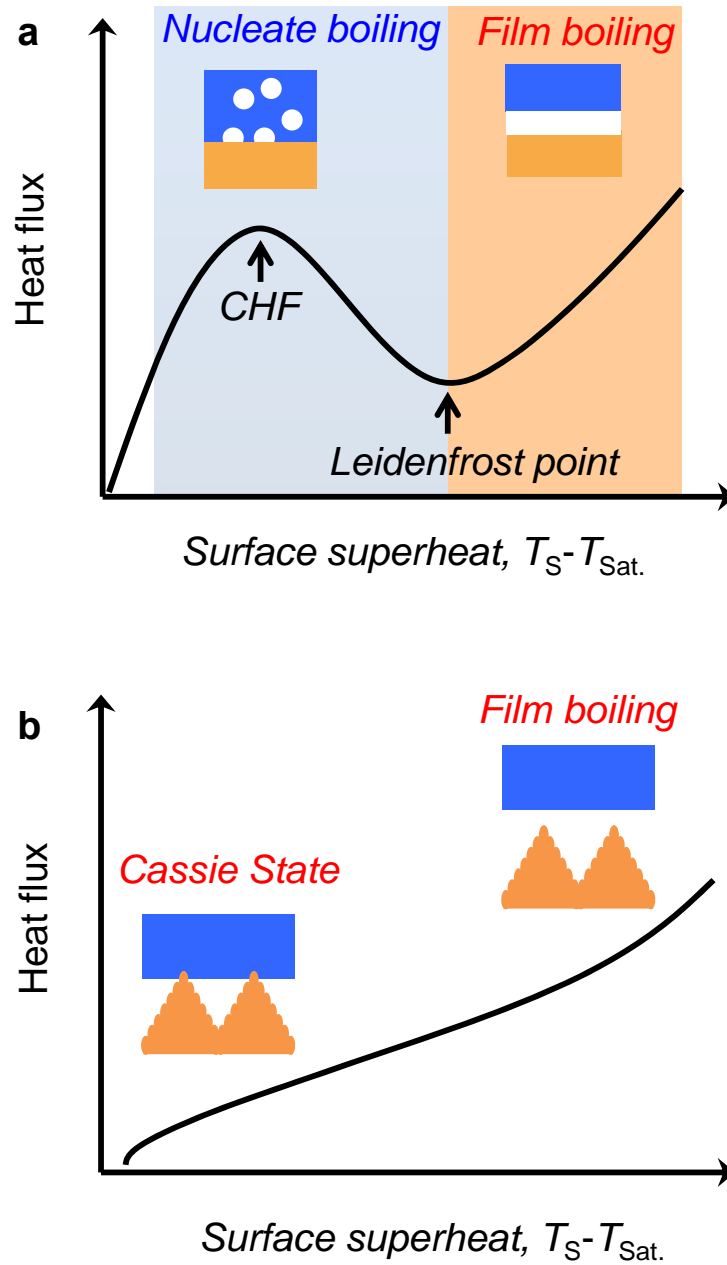
**Supplementary Figure 15. Plate temperature vs. cup surface temperature.**

Plot of plate temperature (proportional to the heat flux) vs. cup surface temperature for the steel cup experimental setup for both hydrophilic (blue) and superhydrophobic (red) surface case.



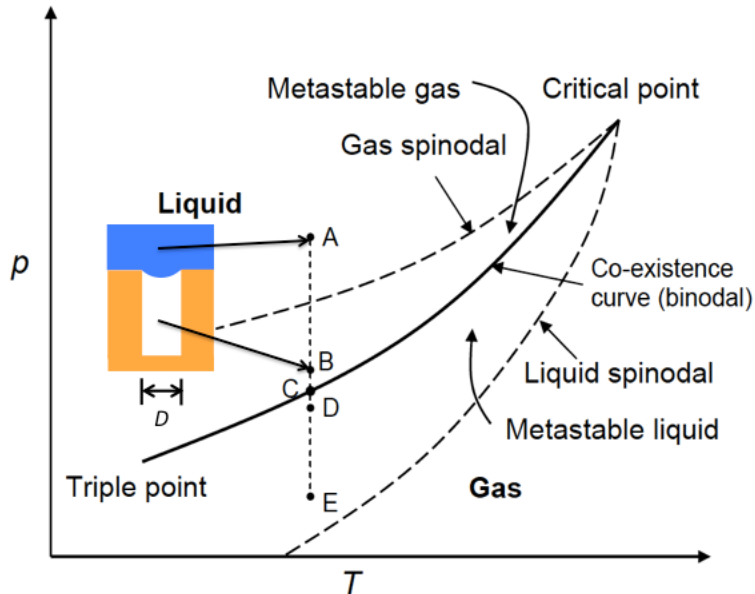
### Supplementary Figure 16. Droplet evaporation time.

Evaporation time of a 100 μl water droplet as a function of the cup surface temperature for the superhydrophobic (solid squares, red) and hydrophobic (open triangles, green) surface case. The Leidenfrost point (LP) temperature for the hydrophobic surface data,  $T_L = 160$  °C is indicated by the arrow.

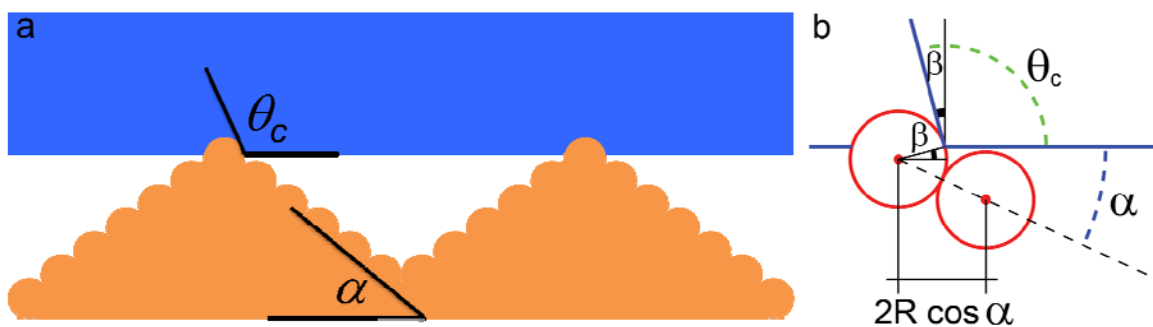


**Supplementary Figure 17. Schematic of the heat flux vs. surface superheat boiling curves.**

(a) Classical boiling curve. (b) Boiling curve for the superhydrophobic surface case.



**Supplementary Figure 18. A typical  $p$ - $T$  diagram for liquid-vapour phase change.** Below the critical point and above the triple point, the phase change line is given by a co-existence or phase change curve. The stable liquid phase is above this curve and the stable vapour phase is below it. On either sides of the co-existence curve are the spinodal curves. Besides the usual stable phases, metastable vapour and liquid phases can also exist in the regions between the spinodal and co-existence curves as shown. At sub-cooled condition a stable liquid (A) should be in chemical equilibrium with a metastable vapour (B) if the vapour state is to be sustained in the pore (inset). Boiling involves phase change of a metastable liquid (E) to a stable vapour (D).



**Supplementary Figure 19. Simplified schematic of pyramidal pillar of nanoparticles.**

(a) A simplified schematic of pyramidal pillar type geometry of the coarse scale roughness. The bumps denote self-assembled spherical nanoparticles.  $\alpha$  is the angle of inclination of the pyramidal pillars and  $\phi$  is local contact angle of a flat liquid-vapour interface. (b) The geometry of two adjacent nanoparticles.